Structures in a Semidilute Polymer Solution Induced under Steady Shear Flow As Studied by Small-Angle Light and Neutron Scattering

Shin Saito and Takeji Hashimoto*

Department of Polymer Chemistry, Graduate School of Engineering, Kyoto University, Kyoto 606-8501, Japan

Isabelle Morfin† and Peter Lindner

Institut Laue-Langevin, BP 156, F-38042 Grenoble Cedex 9, France

François Boué*

Laboratoire Léon Brillouin, CEN Saclay, F-91191 Gif sur Yvette, France

Received December 1, 2000; Revised Manuscript Received October 8, 2001

ABSTRACT: Structures induced by a steady shear flow in a semidilute polymer solution of high molecular weight deuterated polystyrene in dioctyl phthalate are investigated. By a combined use of small-angle light scattering (SALS) and small-angle neutron scattering (SANS), we are able to obtain scattering functions of the shear-induced structures over 3 orders of magnitude in wavenumber (q) and 7 orders of magnitude in intensity. The changes in the structures with shear rate ($\dot{\gamma}$) at a given temperature and with temperature at a given $\dot{\gamma}$ are explored. At a given temperature, the shear flow induces a structural change in the solution at $\dot{\gamma}$ larger than a critical shear rate $\dot{\gamma}_c$, giving rise to a scattering pattern called "butterfly pattern" in the low q region of SANS, while keeping the same pattern as that in the quiescent state in the q region of SALS. As $\dot{\gamma}$ increases, the butterfly patterns evolved not only in the low q region of SANS but also in the q region of SALS. This indicates that the shear-induced structures responsible for the butterfly pattern are developed over a wide q range ($q \leq 0.06$ nm^{-1}) with increasing $\dot{\gamma}$. At a given $\dot{\gamma}$ larger than $\dot{\gamma}_c$, both SALS and SANS scattering intensity increase with a decrease of temperature, indicating the shear-induced structures are more pronounced upon decreasing temperature. Especially, at the lowest temperature covered in this experiment, the scattering pattern observed in the low-q region of SANS is turned into an elliptical shape with a major axis perpendicular to the flow direction, while keeping the butterfly pattern in the SALS q region. A detailed analysis and discussion about the scattering functions are presented in the text.

1. Introduction

Shear-induced enhancement of concentration fluctuations and/or phase separation in a semidilute polymer solution has been extensively explored from the experimental and theoretical points of view. This remarkable phenomenon can be explained by the coupling between concentration fluctuations and stress.[1−4] The most striking feature of this phenomenon was experimentally found in small-angle (SALS) and wide-angle light scattering (WALS) experiments,[5,6] where highly anisotropic scattering patterns with respect to the flow direction were observed. The SALS scattering patterns are called "butterfly patterns" and are characterized by a strong intensity along the flow direction and a "dark streak"[7] perpendicular to the flow direction in the q_x-q_z plane. It was observed[7] that the butterfly patterns appear at $\dot{\gamma}$ larger than $\dot{\gamma}_c$ at a steady state. Here, q is the amplitude of the scattering wave vector defined as $q = |\mathbf{q}| = (4\pi/\lambda)\sin(\theta/2)$, where λ is the wavelength of the incident beam and θ is the scattering angle in medium. x, y, and z indicate flow direction, velocity gradient direction, and vorticity (or neutral) direction, respectively, and q_x, q_y, and q_z denote the respective components of $\mathbf{q}$ along x, y, and z direction, respectively. In the q_x-q_y plane, the WALS experiments of Wu et al. pointed out that the butterfly is distorted around the origin.[6] Some other light scattering experiments have been done to shed light on the time evolution of structures,[8,9] the relaxation mechanism of structures after cessation of shear,[10] and so forth.

The butterfly patterns were also obtained in small-angle neutron scattering (SANS) experiments in the q_x-q_z plane,[11−13] which enables us to observe the shear-induced structures in the length scale from single chain to many chain dimensions. Morfin et al. investigated SANS under continuous shear flow over wide ranges of concentration, temperature, and shear rate, which were analyzed in conjunction with the SALS and the mechanical properties.[11,12] Saito et al. performed the SANS experiments together with SALS under oscillatory shear flow, elucidating that the shear-induced structures become smaller with increasing angular frequency.[13]

As naturally illuminated from the above studies, it turns out to be crucial to elucidate the shear-induced structures over a wide range of length scale for given systems of our interest and hence to measure a structure factor over a wide range of q by scattering techniques for each system of our interest. In this paper, we report our further investigation along this line concerning the structures induced under continuous shear flow at steady state (defined hereafter as steady shear) by a combined use of SALS and SANS. A remarkable difference from the previous study[12] lies in the molecular weight of polymer. Morfin et al. also

† Present address: Lab. de Spectrométrie physique CNRS-UMR5588, UJF, BP 87, 38402 Saint Martin d'Hères, France.

* To whom correspondence should be addressed.

10.1021/ma002051m CCC: $22.00
Published on Web 12/12/2001

employed a PS/DOP solution with almost the same concentration but smaller molecular weight. In their study, the shear-induced structures were relatively smaller than those obtained in this study, and hence detectable SALS scattering was not observed in the range of investigated shear rates. On the contrary, the structures obtained in the present study for a larger molecular weight PS bring about the excess scattering over a wide range of q including SANS and SALS. We can observe the scattering functions over 3 orders of magnitude in q and 7 orders of magnitude in intensity, which would enable us to analyze the shear-induced structures in further detail. It may be worthy of noting that comparisons of scattering with form dichroism, birefringence and others may give useful information on the shear-induced concentration fluctuations and/or phase separation, as reported elsewhere[14] for example. However here in this work we aim to further advance our analysis of the shear-induced structures over a wide length scale ranging from micrometers to nanometers by specially focusing on information expected to be obtained by a combined SALS and SANS technique.

Except for a few experiments, most of the scattering experiments have been conducted in the q_x-q_z plane, because this experimental setup facilitates to detect most accurately quantitative scattering profiles under shear flow. Moreover, this plane is the only plane where up to now SALS and SANS experiments under shear can be connected. It is worthy of noting here that the scattering in q_x-q_z plane and that in q_x-q_y plane should in principle reflect the same physical factors underlying the systems as will be elucidated in Appendix 1.

2. Experimental Methods

2.1. Sample. We used a solution of high molecular weight deuterated polystyrene (d-PS) dissolved in dioctyl phthalate (DOP). The d-PS used was prepared by living anionic polymerization[15] and had a weight-average molecular weight (M_w) of 2.0×10^6, which was determined by dynamic light scattering. The solution containing d-PS by 8.0 wt % was prepared by dissolving a prescribed amount of d-PS and DOP in excess of dichloromethane and by evaporating dichloromethane completely. DOP is a Θ solvent for d-PS. The Θ temperature has been measured for d-PS of lower molecular weight in DOP and was found equal to 7 °C:[12] the same value should apply here. The solution is in the semidilute regime; the concentration c satisfies $c/c^* = 6.4$, c^* being the overlap concentration.[16] The cloud point T_{cl} of this solution has not been determined, but all the experiments in this paper were carried out above T_{cl} since the system at rest remained clear at the lower temperature used (12 °C).

2.2. Small-Angle Light Scattering. A cone and plate flow cell, described elsewhere,[17] enabled us to carry out simultaneous measurements of flow SALS, optical microscopy, and rheological properties. Figure 1a shows a schematic diagram of this flow SALS apparatus, where the x-, y-, and z-axis respectively correspond to the flow direction, the velocity gradient direction, and the vorticity (neutral) direction, as said already above. The shear cell consists of a cone and plate made of quartz with radii of 40 mm and a cone angle of 1°. It is covered by an enclosure in which temperature is controlled with an accuracy of ±0.3 °C. A He−Ne laser with a wavelength of 632.8 nm was used as an incident beam source. The incident beam propagates along the velocity gradient direction. The scattered light was detected by a cooled charge coupled device (CCD) camera as a two-dimensional detector, the detecting plane of which is set parallel to Oxz-plane. The accessible q range is between $q_{min} = 6.27 \times 10^{-4}$ nm^{-1} and $q_{max} = 3.63 \times 10^{-3}$ nm^{-1} (see Figure 1b).

The two-dimensional data were sector-averaged parallel to the flow direction with the azimuthal angle of ±5° and perpendicular to the flow direction with ±2°. We also evaluated the sector-averaged data at quiescent state. Then the scattering excess from the quiescent state was obtained by subtracting the scattering under shear flow from the scattering in the quiescent state. This does not give the scattering in absolute units but has the advantage of getting rid of the intensity scattered by the shear cell itself.

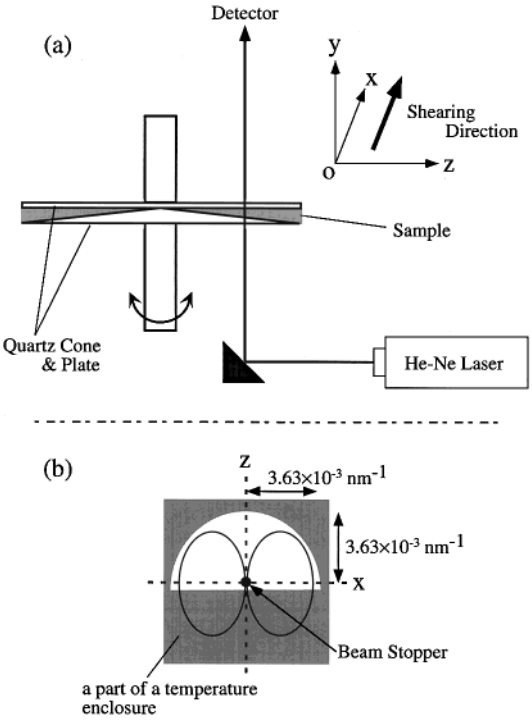

Figure 1. (a) Schematic diagram of the SALS setup. The Ox axis is parallel to the flow direction, the Oy axis to shear gradient direction, and the Oz axis to the vorticity or neutral direction. The incident beam was sent along the Oy axis, and the two-dimensional scattering pattern is detected by CCD camera with its detector plane set parallel to the Oxz plane. (b) Due to the optical setup, the q range for scattered light is limited inside the half circle with the radius of $q = 3.63 \times 10^{-3}$ nm^{-1}. The half-circle corresponds to a window opened up in the temperature enclosure for the SALS observation.

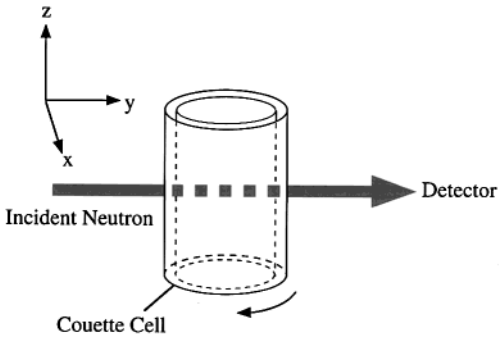

Figure 2. Schematic diagram of the SANS set up. x, y, and z axes have the same definitions as those in Figure 1. The incident neutron beam is sent along the velocity gradient direction (along the y direction), by which we can access the same plane as the SALS experiment.

2.3. Small-Angle Neutron Scattering. Small-angle neutron scattering experiments under steady shear flow were performed at the instrument D11 of the Institut Laue-Langevin ILL, Grenoble, France. Figure 2 shows the schematic diagram of the sample cell and the geometry of the experimental setup. The definition of x-, y-, and z-direction (with respect to the velocity and velocity gradient directions) is the same as that described in the SALS setup. However, instead

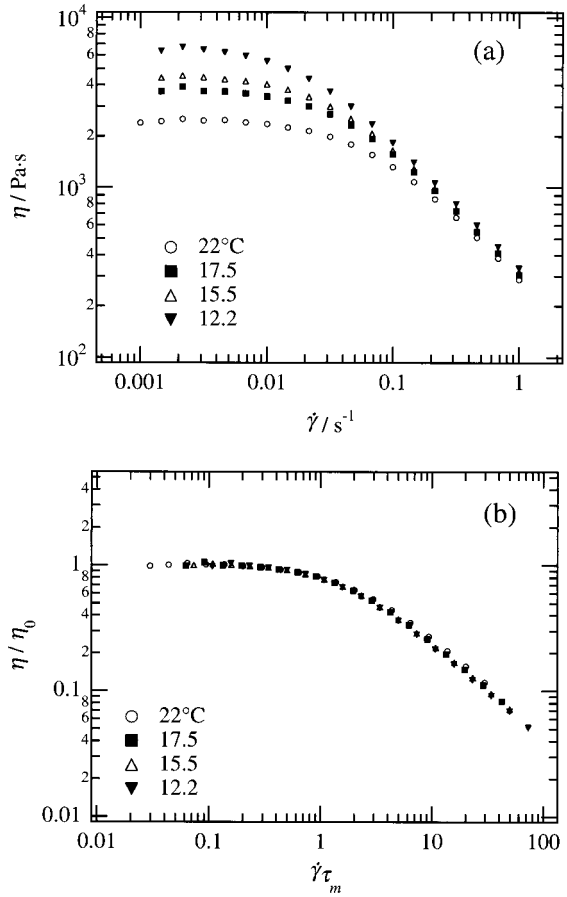

Figure 3. (a) Steady-state viscosity η at 22, 17.5, 15.5, and 12.2 °C as a function of $\dot{\gamma}$. (b) The reduced plot of η with η/η_0 as a vertical axis and $\dot{\gamma}\tau_m$ as a horizontal axis. η_0 and τ_m, the zero-shear viscosity and the maximum relaxation time, respectively, are summarized in Table 1.

of a cone and plate, we use a Couette cell made of quartz to impose the steady shear flow; the details of this cell have been described elsewhere.[18] The temperature is controlled by circulation of water in compartments placed inside the inner cylinder on either side of the beam path. The neutron beam passes through the sample in the direction parallel to the velocity gradient direction, which enables us to observe the SANS in the same plane (the $x-z$ plane) as the SALS experiment. With the wavelength of 10 Å and the sample-to-detector distance of $L = 2.5$, 10, and 35.7 m, the effective q range of $6.76 \times 10^{-3} \leq q \leq 7.75 \times 10^{-1}$ nm^{-1} was covered in this experiment.

The data were corrected for the detector background and the empty cell scattering. We obtained the coherent differential scattering cross section $d\Sigma/d\Omega(\mathbf{q})$ in the absolute units (cm^{-1}) by calibrating observed scattering cross section with that from 1 mm thick water sample. The data were sector-averaged in the direction parallel to the flow over an angular sector of 30° and in the direction perpendicular to the flow over an angular sector of 15° to obtain scattering cross sections (scattering intensity) as a function of q_x or q_z.

2.4. Rheology. Measurement of the steady-state viscosity as a function of the shear rate $\dot{\gamma}$ was carried out with ARES-FS (Rheometric Scientific Co. Ltd.) by using a temperature-controlled cone−plate fixture with radii of 25 mm and a cone angle of 0.04 rad.

3. Results

3.1. Rheological Properties. Figure 3a shows the steady-state viscosity η as a function of $\dot{\gamma}$ obtained at 22, 17.5, 15.5, and 12.2 °C. At $\dot{\gamma}\tau_m < 1$, where τ_m is the maximum relaxation time, η remains close to the value obtained in the linear regime ($\dot{\gamma}\tau_m \ll 1$), and at $\dot{\gamma}\tau_m > 1$, η shows the shear-thinning behavior.

Table 1. Temperature Dependence of Viscoelastic Properties

T/C°	τ_m/s	η_0/Pa·s
12.2	73.2	6.50×10^2
15.5	50.1	4.43×10^2
17.5	42.2	3.70×10^2
22.0	29.7	2.45×10^2

From these viscoelastic data, we determine τ_m and the zero-shear viscosity η_0, which are summarized in Table 1. These are obtained by the fitting with a Carreau function[19]

$$\eta = \eta_0[1 + (\dot{\gamma}\tau_m)^2]^{-a} \quad (1)$$

where a is a shear-thinning exponent. In Figure 3b, the normalized plots of the steady-state viscosity are presented with η/η_0 as a vertical axis and $W_i = \dot{\gamma}\tau_m$, the Weissenberg number as a horizontal axis. It is important to note that these data obtained at various temperatures are falling onto a single master curve (time−temperature superposition).

3.2. $\dot{\gamma}$ Dependence of SALS and SANS at a Given Temperature. 3.2.1. 2D Patterns. Figure 4 shows the $\dot{\gamma}$ dependence at 22 °C of SALS and SANS patterns obtained at different sample−detector distances L. We recall that the larger the value of L, the lower the q region we can access.

At quiescent state (i.e., $\dot{\gamma} = 0$ s^{-1}), both the SALS and SANS patterns are isotropic and their intensities are weak. At $\dot{\gamma} = 0.1$ s^{-1}, there is no change in shape and intensity compared to the quiescent state: the shear flow does not affect the concentration fluctuations. At $\dot{\gamma} = 0.2$ s^{-1}, only SANS at $L = 35.7$ m ($6.76 \times 10^{-3} \leq q \leq 6.00 \times 10^{-2}$ nm^{-1}) shows an anisotropic pattern with a strong intensity along the flow direction (often called a butterfly pattern) without any change in the q_z direction. This indicates a large amplitude of concentration fluctuations developed only along the flow direction in the q range covered. In larger ($2.51 \times 10^{-2} \leq q \leq 8.00 \times 10^{-1}$ nm^{-1}) and lower q regions ($6.27 \times 10^{-4} \leq q \leq 3.63 \times 10^{-3}$ nm^{-1}) covered by SANS and SALS, respectively, the shapes and the intensities are almost the same as those in quiescent state, indicating that the structures are not affected much by shear flow in the two corresponding q ranges.

At $\dot{\gamma} = 0.4$ s^{-1}, the SALS pattern also begins to exhibit the butterfly pattern, indicating that the concentration fluctuations expand to larger length scales. At higher shear rates ($\dot{\gamma} = 1$ and 2.6 s^{-1}), both the SALS and SANS butterfly patterns evolve in such a way that the scattering intensity along the flow direction increases and the butterfly wings expand, resulting in sharpening of the dark streak perpendicular to the flow direction. On the contrary, the SANS patterns obtained at short distances ($L = 10$ and 2.5 m) remain equal to those at the quiescent state: the concentration fluctuations reflected in this q region ($2.51 \times 10^{-2} \leq q \leq 7.75 \times 10^{-1}$ nm^{-1}) are not enhanced at these $\dot{\gamma}$.

3.2.2. Intensity Profiles. To estimate the scattering intensity more quantitatively, we shall focus on the scattering profiles parallel and perpendicular to the flow direction. Figure 5 shows the $\dot{\gamma}$ dependence of the SALS and SANS profiles parallel ((a) $I(q_x)$, top) and perpendicular ((b) $I(q_z)$, bottom) to the flow direction. These

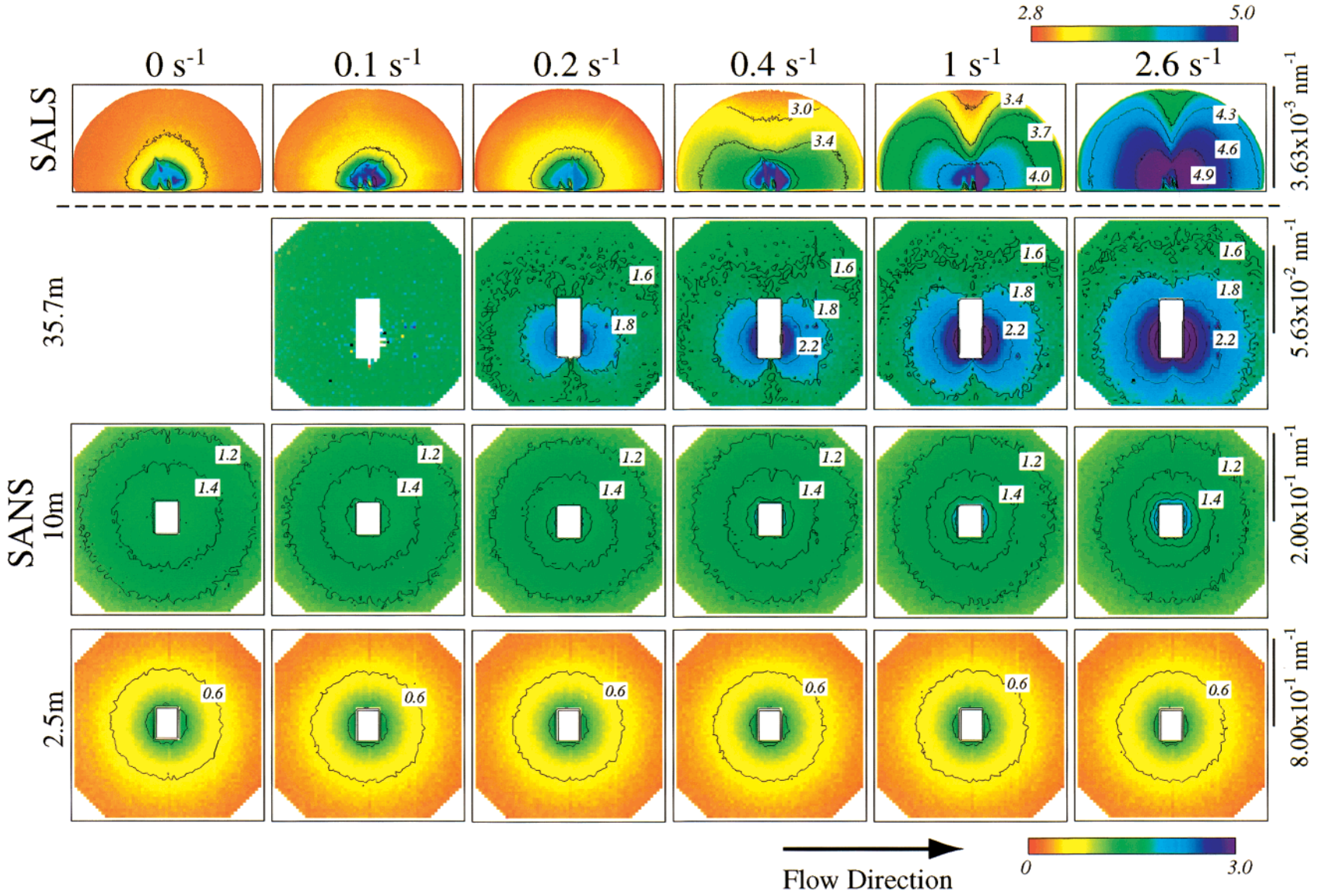

Figure 4. SALS and SANS patterns obtained at the shear rates from 0 to 2.6 s^{-1} at a given temperature of 22 °C. The SANS patterns obtained at the different L (35.7, 10, and 2.5 m) are presented. The color bars for the scattering intensity are shown on the logarithmic scale. The values attached on the color bars (absolute unit in SANS and arbitrary unit in SALS) are the upper and lower limits (from $10^{2.8}$ to $10^{5.0}$ arbitrary units for SALS and from 10^{0} to $10^{3.0}$ cm^{-1} for SANS) of the color histograms. The scale bars attached to the respective SANS patterns indicate a q scale of 5.63×10^{-2} nm^{-1} for 35.7 m, 2.00×10^{-1} nm^{-1} for 10 m, and 8.00×10^{-1} nm^{-1} for 2.5 m, while that attached to the SALS pattern indicates a q scale of 3.63×10^{-3} nm^{-1}.

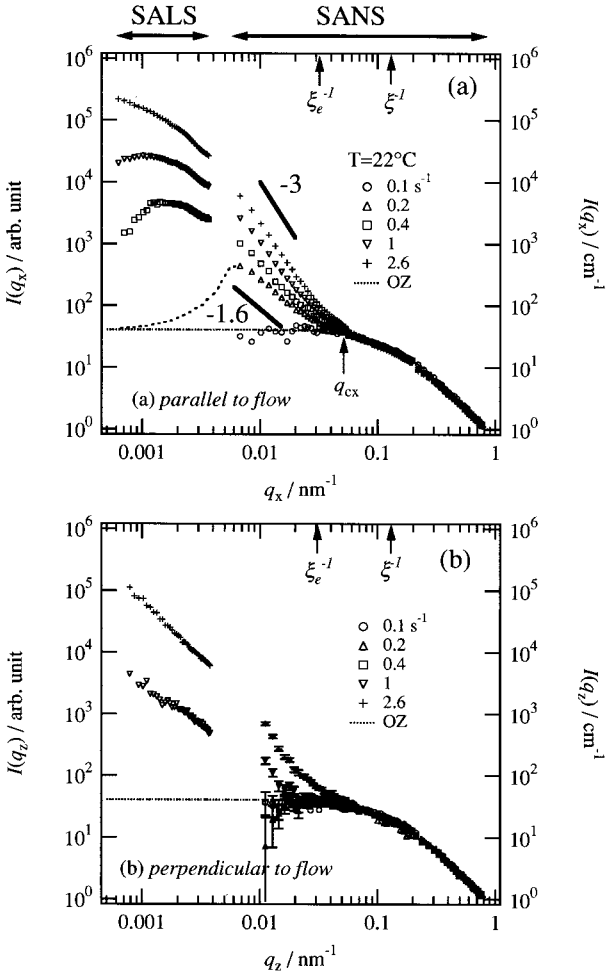

Figure 5. SALS (scale on left ordinate axis) and SANS (right ordinate axis) profiles parallel (the top (a)) and perpendicular (the bottom (b)) to the flow direction measured at various shear rates and at a given temperature, 22 °C. The SALS profiles were equally multiplied by a shift factor in order to compare them with SANS profiles, although the SANS profiles are shown in the corrected absolute intensity scale (cm^{-1}).

were evaluated from the two-dimensional scattering patterns presented in Figure 4. An Ornstein−Zernicke (OZ) function obtained by fitting the SANS profile from the solution at rest is also included (see dotted lines). The OZ function defined by

$$I_{OZ}(q) = \frac{I_{OZ}(q=0)}{1 + q^2\xi^2} \tag{2}$$

reflects the concentration fluctuations in a single phase where ξ is the correlation length of the thermal concentration fluctuations.

There is a small gap in q scale between the lower q limit of SANS and the higher q limit of SALS. The SALS intensities (left ordinate axis) at different $\dot{\gamma}$ were equally multiplied by a shift factor in order to compare them with the SANS scattering cross sections (right ordinate axis). Representative error bars (when larger than the symbol size) are shown in Figure 5b since there is more space available than in Figure 5a.

Profiles along q_x. Let us first focus on $I(q_x)$ (Figure 5a). At $\dot{\gamma} = 0.2$ s^{-1}, the excess scattering from the OZ intensity level from the solution at rest exists in the low-q region of SANS ($q < 0.06$ nm^{-1}). It is worth noting that the SANS profile shows the power law with an exponent of about −1.6. Such a shape of the SANS profile may infer existence of some excess scattering in the SALS q region; however, we could not observe it. This is probably because the scattered signal is too weak to be detected with our SALS apparatus. This means that it is close to the signal at rest that can be extrapolated from the OZ function obtained in the SANS q range. Thus, we expect a maximum in the scattering as shown by the dashed line (which is only a visual guide) at a q value between the SALS and SANS q ranges.

With a further increase of $\dot{\gamma}$, reaching $\dot{\gamma} = 0.4$ s^{-1}, both the SALS and SANS intensities increase. Maxima in the SALS scattering are clearly recognized at 0.4 s^{-1} as well as at 1 s^{-1} for $I(q_x)$. This means that a periodic structure with a characteristic length exists. With increasing $\dot{\gamma}$, the position of the scattering maximum, defined as q_{mx}, moves toward smaller q and the peak intensity, defined as I_{mx}, increases, indicating the shear-induced structures are coarsened in terms of both amplitude and characteristic length of concentration fluctuations. At 2.6 s^{-1}, no scattering maximum is visible in the q region covered by SALS, but it is naturally expected that it would exist in the q region less than 6×10^{-4} nm^{-1}. Another possibility is that it is hidden by some parasitic low-q signal. The evidence for the low-q shift of the peak position with $\dot{\gamma}$ may seem weak to readers. However, we are confident in this shift of q_{mx}, because the same but more clear trends were found to other PS/DOP systems with different molecular weights, concentrations, and temperatures.[20]

There is another common feature in all SANS profiles of Figure 5a which is very impressive: there is a critical q almost independent of $\dot{\gamma}$ (defined as q_{cx}), below which the intensity increases with $\dot{\gamma}$ but above which the intensity is almost the same as the OZ level from the solution at rest. These observations will be discussed later in section 5.4. In the former q region, the intensity $I(q_x)$ shows the power law with respect to q_x, $I(q_x) \sim q_x^{-\alpha}$, with the exponent α between 1.6 and 3, which gradually increases with an increase of $\dot{\gamma}$.

Profiles along q_z. We next pay attention to $I(q_z)$ (Figure 5b). At $\dot{\gamma}$ below 0.4 s^{-1}, there is no excess scattering in both SALS and SANS from the quiescent state. At $\dot{\gamma} = 1$ and 2.6 s^{-1}, both the SALS and the SANS intensities increase with $\dot{\gamma}$ for $q < 6 \times 10^{-2}$ nm^{-1}.

Comparison between Profiles along q_x and q_z. To compare $I(q_x)$and $I(q_z)$ at the same $\dot{\gamma}$, the scattering profiles shown in Figure 5 are replotted in Figure 6. For all $\dot{\gamma}$, in the q region less than about 0.06 nm^{-1} (marked by arrows), $I(q_x)$ exceeds $I(q_z)$, indicating that anisotropic structures having a large amplitude of concentration fluctuations along the flow direction are formed in this q scale. However, when $\dot{\gamma}$ is increased, the increment of $I(q_z)$ with $\dot{\gamma}$ is larger than that of $I(q_x)$, resulting in a gradual approach of $I(q_z)$ to $I(q_x)$.

3.3. Temperature Dependence of SALS and SANS at a Given $\dot{\gamma}$. 3.3.1. 2D Patterns. Figure 7 shows the temperature dependence of the SALS and SANS patterns obtained at $\dot{\gamma} = 2.6$ s^{-1}. These were measured as follows: after the scattering patterns were taken at 22 °C and $\dot{\gamma} = 2.6$ s^{-1}, the temperature was decreased toward 17.5 °C, while keeping $\dot{\gamma} = 2.6$ s^{-1}. After the system reached the steady state, the scattering patterns were measured again at this condition. We iterated this procedure to obtain the scattering patterns at lower

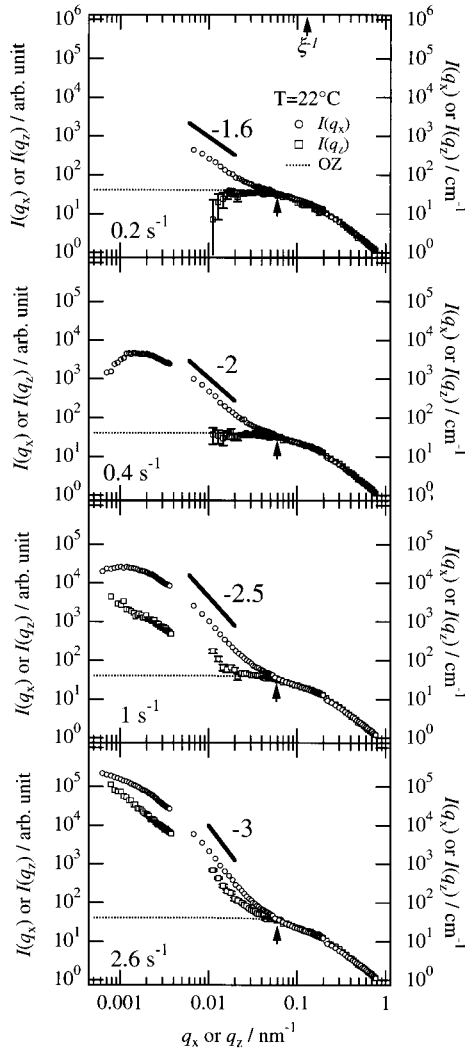

Figure 6. Comparison of the scattering profiles parallel and perpendicular to the flow direction at the various values of $\dot{\gamma}$.

temperatures in decreasing order: first 15.5 °C and then 12.2 °C. Note that this second series of experiments shown in Figure 7 can be considered as a direct continuation of the first one: it corresponds to a further increase of the Weissenberg number W_i compared to the first one at $\dot{\gamma} = 2.6$ s^{-1} and $T = 22$ °C in Figure 4, decreasing T being another way to increase W_i.[12]

At 22 °C, we can observe the butterfly patterns in the SALS as well as in the SANS at $L = 35.7$ m, which have been already presented in the right column in Figure 4. At 17.5 °C, the SALS patterns strengthen, meanwhile the SANS butterfly patterns at $L = 35.7$ m change in shape: since the scattering intensity perpendicular to the flow direction increases, and the two lobes of the butterfly seem closer to one another, leading to less well-defined butterfly shape.

These trends become more obvious with decreasing further the temperature to 15.5 and 12.2 °C: on one hand, the butterfly observed in SALS is further developed, resulting in an extremely sharp dark streak. On the other hand, the characteristic of the butterfly disappears in SANS at $L = 35.7$ m: the two lobes are now merged into an elliptical pattern with a major axis perpendicular to the flow direction. The SANS intensity level at $L = 10$ m increases a little with decreasing the temperature, and at 12.2 °C this 10 m pattern also becomes elliptical with a major axis perpendicular to the flow direction. On the contrary, there is no change in the SANS pattern at $L = 2.5$ m through this experiment.

3.3.2. Profiles along q_x and q_z. Figure 8 shows the temperature dependence of the SALS and SANS profiles parallel and perpendicular to flow, as evaluated from the 2D scattering patterns of Figure 7. The SALS intensities were all multiplied by the same shift factor as that applied in Figures 5 and 6, although these are different measurements. This is a good check of our procedure. In the SANS q region less than about 0.1 nm^{-1}, the scattering intensity for both direction increases with keeping the power law exponent α of 3 as temperature decreases. The q range where the $\alpha = 3$ power law is retained in $I(q_x)$ is wider than that in $I(q_z)$. In the SALS q region, the scattering intensity also increases with decreasing temperature, whereas no scattering maximum is observed in the q range covered in this SALS and SANS experiment.

Comparison between the scattering profiles $I(q_x)$ and $I(q_z)$ (Figure 9) shows that the gradual approach of $I(q_z)$ to $I(q_x)$ observed with an increase of $\dot{\gamma}$ at 22 °C (see Figure 6) continues with a decrease of T. For 17.5 and 15.5 °C, $I(q_x)$ and $I(q_z)$ are very close to overlap. Let us note however that such similarity in the parallel and perpendicular directions does not exclude some differences in oblique directions and therefore the persistence of an anisotropy. Eventually, at $T = 12.2$ °C, $I(q_z)$ exceeds $I(q_x)$ in the low-q region of SANS, which corresponds to the change in 2D pattern into the elliptical shape with its major axis oriented along z direction.

4. Analysis

4.1. Variations with $\dot{\gamma}$. The combination of SALS data with SANS data in steady-state shear presented in this paper (Figures 4−6) should help us to elucidate the evolution of the steady-state structures with $\dot{\gamma}$, together with data obtained in previous series of works, first on SALS[5,7] and then on SANS.[12,13]

4.1.1. Comparison with Former SALS Results. In former results,[7] the dependence of the SALS behavior on $\dot{\gamma}$ has been classified into four regimes. The first two regimes are observed here also: regime I at $\dot{\gamma} < \dot{\gamma}_c$, where concentration fluctuations are identical with those at the quiescent state, and regime II at $\dot{\gamma} > \dot{\gamma}_c$, where butterflies appear and expand. Even in regime II, when $\dot{\gamma}$ increases beyond a certain value, defined hereafter $\dot{\gamma}_{c,demix}$, $I(q_z)$ starts to increase. $\dot{\gamma}_{c,demix}$ depends on molecular weight, concentration, solvent, and temperature. Regimes I and II are observed also for the present SALS data.

Conversely, the two subsequent regimes observed formerly[7] are not present here: in regime III, $I(q_x)$ reaches a constant value with $\dot{\gamma}$, while $I(q_z)$ still increases. In regime IV (at $\dot{\gamma} > \dot{\gamma}_a$, where subscript "a" stands for anomalous behavior), $I(q_x)$ and $I(q_z)$ further increase and a strong bright streaklike pattern oriented perpendicular to the flow direction appears, which is overlapped on the highly developed butterfly pattern. This streaklike scattering pattern is originated in the formation of the string phase elongated parallel to the flow direction.[14] In this regime, the scattering anomaly is accompanied by rheological anomalies, which are found in the intense instabilities or fluctuations of the steady-state viscosity η and the first normal stress difference N_1.

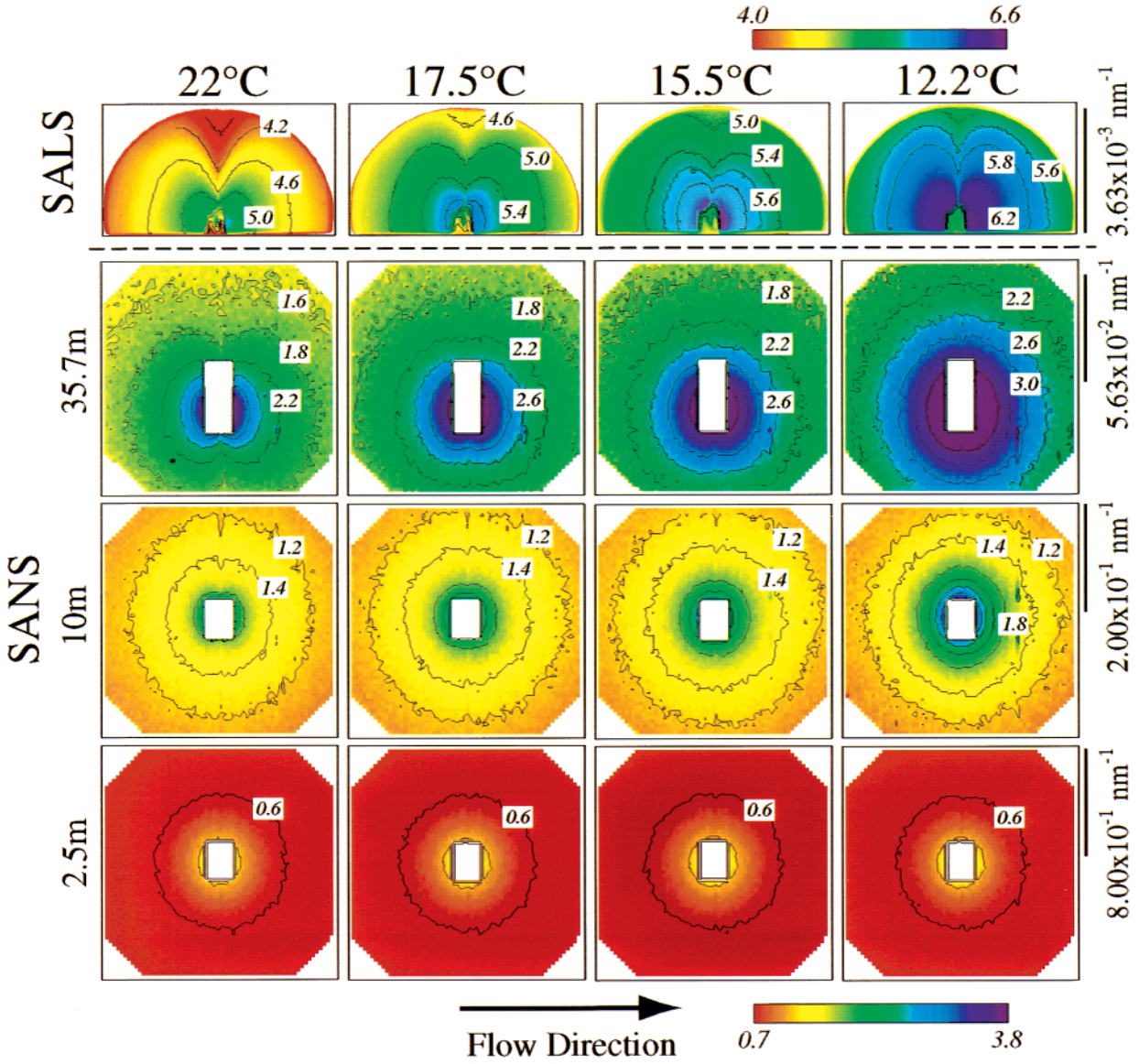

Figure 7. SALS and SANS patterns obtained at the temperatures from 22 to 12.2 °C at a given shear rate of 2.6 s^{-1}. The color bars for the scattering intensity are shown in the logarithmic scale. The values attached on the color bars (absolute unit in SANS and arbitrary unit in SALS) are the upper and lower limits (from $10^{4.0}$ to $10^{6.6}$ arbitrary units for SALS and from $10^{0.7}$ to $10^{3.8}$ cm^{-1} for SANS) of the color histograms.

The fact that regimes III and IV are not observed in this experiment for the particular solution studied here is certainly due to the limited $\dot{\gamma}$ range covered: the shear flow with the Couette cell used in the SANS experiment here brings the Weissenberg instability at lower $\dot{\gamma}$ than that with the cone and plate used in the former SALS experiment and therefore do not allow the observation of strong shear effect. In addition, we used a low molecular weight and a relatively higher temperature (here, $T > \Theta$ since the deuteration of PS lowers the Θ temperature of the h-PS/DOP solution from 22 to 7 °C[12]) compared to the previous SALS experiments. This implies a shorter relaxation time of the solution of the present study and therefore a lower shear effect for a given $\dot{\gamma}$.

4.1.2. Comparison between SALS and SANS Critical Shear Rates $\dot{\gamma}_{c,SALS}$ and $\dot{\gamma}_{c,SANS}$. The evolution of the scattering in SANS and SALS seems to be shifted in terms of threshold in $\dot{\gamma}$. At $T = 22$ °C and $\dot{\gamma} = 0.1$ s^{-1} ($W_i = 2.97$) no change, compared with the quiescent state, is observed in the patterns and profiles of SALS and SANS (Figures 4 and 5). At 0.2 s^{-1}($W_i = 8.44$), Figure 4 shows clearly the butterfly pattern in the small-q region of SANS at $L = 35.7$ m while the SALS shows no change (Figure 4).

A clear determination of this threshold $\dot{\gamma}_c$ is given in Figure 10 where the integrated intensity at a given $\dot{\gamma}$, $\mathcal{T}_{K,J}(\dot{\gamma})$, relative to that at $\dot{\gamma} = 0$ s^{-1}, $\mathcal{T}_{K,J}(\dot{\gamma}=0)$, is plotted as a function of $\dot{\gamma}$, with K being either SANS or SALS and J being either along q_x or q_z defined by

$$\mathcal{T}_{K,q_x}(\dot{\gamma}) = \int_{q_{x,\min}}^{q_{x,\max}} I_K(q_x;\dot{\gamma})\, dq_x \qquad (3)$$

$$\mathcal{T}_{K,q_z}(\dot{\gamma}) = \int_{q_{z,\min}}^{q_{z,\max}} I_K(q_z;\dot{\gamma})\, dq_z \qquad (4)$$

where $q_{x,\min}$ and $q_{x,\max}$ are the lower and upper limits of the experimental q window (for SALS or for SANS) along q_x and the same for $q_{z,\min}$ and $q_{z,\max}$. Note that the scattering intensity used for the calculation of $\mathcal{T}_{SALS,J}(\dot{\gamma})$ is that before subtracting the background intensity $I_b(q)$, i.e., $I(q) + I_b(q)$.

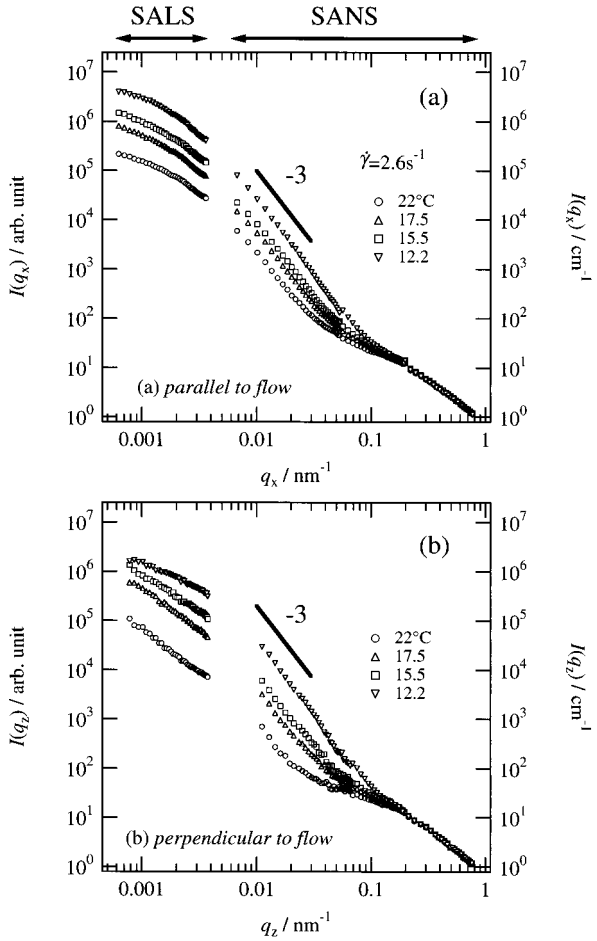

Figure 8. SALS (the left ordinate axis) and SANS (the right ordinate axis) profiles parallel (the top (a)) and perpendicular (the bottom (b)) to the flow direction measured at various temperatures and at a given shear rate, $\dot{\gamma} = 2.6$ s^{-1}. The SALS profiles were equally multiplied by the same shift factor as that in Figure 5.

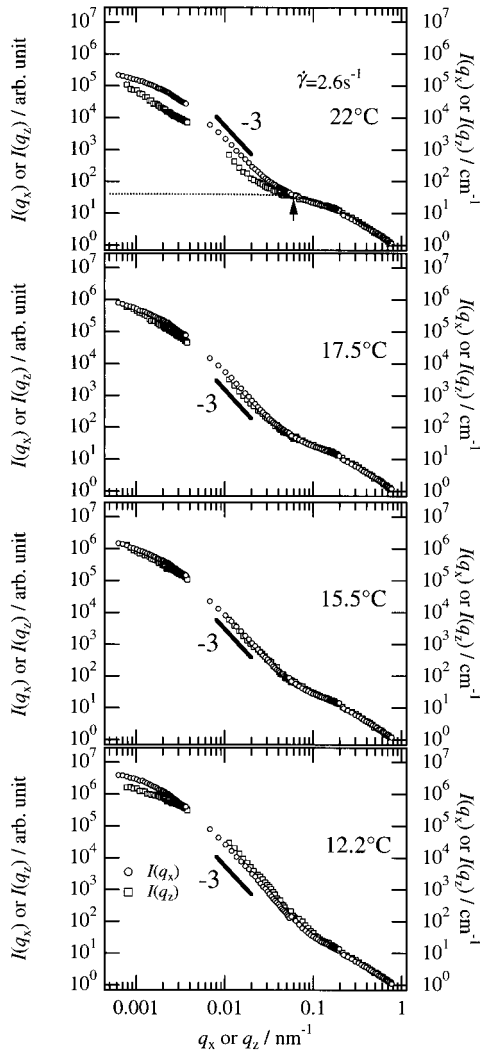

Figure 9. Comparison of the scattering profiles parallel and perpendicular to the flow direction at various temperatures at $\dot{\gamma} = 2.6$ s^{-1}.

We see neatly that the apparent threshold $\dot{\gamma}_c$ is lower for SANS than for SALS. A first explanation can be that the detection sensitivity for SALS might be less than that for SANS. A second explanation can be that the large length scale structures which are seen in the SALS q range develop at higher $\dot{\gamma}$. The latter explanation is supported by previous experiments[12] with a lower molecular weight solution for which structure under shear was visible only by SANS in a wide range of shear rates before to be seen by SALS. In our present study, the maximum in the scattering as anticipated in Figures 5 and 6 credits also this hypothesis.

Let us note that the corresponding threshold values of W_i, $W_{i,c}$, obtained here ($W_{i,c} \sim 4$ for SANS and $\sim$9 for SALS) are slightly above $W_i \sim 1$, where $W_{i,c}$ is the critical Weissenberg number predicted by models described later for the butterfly formation.

We can also define another critical shear rate directly from the shape of the intensity: for example, the threshold above which $I(q_z)$ or $\mathcal{T}_{K,q_z}(\dot{\gamma})$ shows the value greater than $I(q_z,\dot{\gamma}=0)$ or $\mathcal{T}_{K,q_z}(\dot{\gamma}=0)$ (Figures 5b, 6, and 10), which occurs at $W_i = 8.44$ (for SANS data) reflects a nonlinear effect of the shear flow. We will note this threshold $\dot{\gamma}_{c,\mathrm{demix}}$, since it may well represent the onset of demixing: above $\dot{\gamma}_{c,\mathrm{demix}}$, the exponent α approaches the constant value of 3 in both q_x and q_z directions (Figures 5 and 8), suggesting a quasi-two-phase structure (section 4.3.3).

4.1.3. Shear Rate Dependence of the Scattering Maximum. If $\dot{\gamma}$ is increased, the development of the butterfly pattern exhibits the trend observed in regime II: the intensities of the butterflies in SALS and SANS increase and the butterfly wings expand with $\dot{\gamma}$ (Figure 4).

In addition, a scattering maximum appears parallel to the flow direction in the SALS q region (Figures 5 and 6). Let us note that we obtain the maximum in two cases only (one where the intensity along q_z has not yet increased (0.4 s^{-1}), one where it has 1 s^{-1}). As $\dot{\gamma}$ increases, q_{mx} decreases (the peak moves toward low q_x with $\dot{\gamma}$, i.e., the associated characteristic size increases) and I_{mx} increases. The fact that the low-q shift of q_x with $\dot{\gamma}$ is a reliable and convincing evidence was already commented in section 3.2.2.

The trend of the pattern evolution and the changes in q_{mx} and I_{mx} indicate that the shear-induced structures develop with increasing $\dot{\gamma}$: the higher the shear rate, the clearer the structure and the larger the characteristic size.

In the scheme of the solvent squeeze model as detailed elsewhere,[21] the larger the shear rate, the greater the buildup of the elastic free energy and hence the more the solvent is squeezed from the more entangled regions for relaxation of the elastic free energy buildup. This

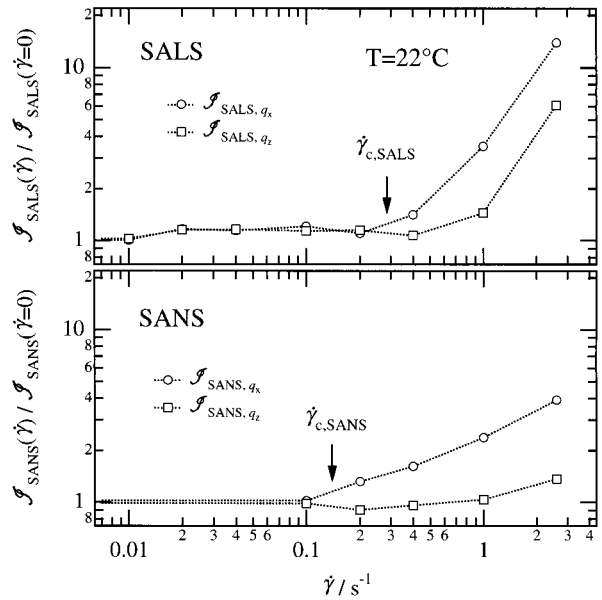

Figure 10. Integrated intensity, $\mathcal{I}_{K,J}(\dot{\gamma})/\mathcal{I}_{K,J}(\dot{\gamma}=0)$, as a function of $\dot{\gamma}$, where K designates SALS or SANS and J designates q_x or q_z, $q_{x,\min}$ (6.27×10^{-4} nm^{-1} for SALS and 6.76×10^{-3} nm^{-1} for SANS), and $q_{x,\max}$ (3.63×10^{-3}nm^{-1} for SALS and 7.75×10^{-1} nm^{-1} for SANS) are the lower and upper limits of the experimental q window along q_x, and $q_{z,\min}$ (7.82×10^{-4} nm^{-1} for SALS and 1.12×10^{-2} nm^{-1} for SANS) and $q_{z,\max}$ (3.76×10^{-3} nm^{-1} for SALS and 7.63×10^{-1} nm^{-1} for SANS) are the lower and upper limits of the experimental q window along q_z. Note that the scattering intensity used for the calculation of $\mathcal{I}_{SALS,J}(\dot{\gamma})$ is that before subtracting the background intensity $I_b(q)$, i.e., $I(q) + I_b(q)$.

driving force leads to the formation of larger structures with great amplitude of concentration fluctuations under shear.

4.1.4. Comparison with Low Molecular Weight SANS Data. Here we shall make a comparison between present SANS data and previous one obtained by Morfin et al.[12] They also used a d-PS/DOP solution, of similar concentration (9%), but lower M_w of 5.72×10^5. Both solutions exhibit almost the same SANS patterns in the quiescent state, with similar values of the correlation length.

Under shear, the signal changes at large q are really similar for the two solutions; however, the q regime where shear effect appears was located in a higher q region in ref 12 than in our experiment. This means that the shear-induced structure takes place at larger length scale for our higher molecular weight.

There is another difference to note: for $q_x > q_{cx}$, $I(q_x;\dot{\gamma}) < I(q_x;\dot{\gamma}=0)$ was observed with the low molecular weight sample; i.e., the chains are more elongated than in the quiescent state. So everything works as if for large molecular weight coarser structures are created sooner, and more easily, allowing for less deformation of the chains.

Let us note finally that the SANS scattering cross section for smaller M_w was fitted with the sum of a Ornstein−Zernike function and a square Lorentzian function in the parallel direction: we will see below that a slightly different function is used here for larger M_w.

4.2. Variations with Temperature. The two-dimensional pattern evolution with decreasing temperature at the highest shear rate studied indicates that a decrease of temperature induces a further development of the shear-induced structures. Like for rheological measurements, we might say that increasing $\dot{\gamma}$ at a given temperature and decreasing temperature at a given $\dot{\gamma}$ are equivalent, following the time−temperature superposition principle. However, we have seen in the former SANS experiments[12] that this superposition was not obeyed regarding the scattering information. At lower temperature, the system is more sensitive to shear for a same W_i. This means that decreasing temperature affects two properties of the solution, that is, not only the rheological properties but also the thermodynamic state of the solution. This important fact observed by SANS[12] is now confirmed here by light scattering.

Our aim in this work is only to illuminate the fact that lowering the temperature enhances the shear-induced effects but not to explore precisely the effects of these two properties on the shear-induced structures. Comparison and separation of these two effects will be left as a future work.

4.3. Decomposition of a Scattering Profile into Two Contributions: OZ, SQL, and Modified SQL. Here we focus on an asymptotic behavior of the scattering profiles only at $q_x > q_{mx}$, rather than the scattering behavior in a whole q range, and attempt to give a phenomenological description of the scattering functions. However, the prediction of the scattering functions themselves based on statistical mechanical models are beyond the scope of this work. For the phenomenological description, we try to decompose the scattering profiles at $q_x > q_{mx}$ shown in Figures 5, 6, 8, and 9 into two scattering functions. Indeed, for $\dot{\gamma} > \dot{\gamma}_{c,demix}$, such decomposition is strongly suggested by the shape of the scattering.

4.3.1. OZ with a SQL Function. Assuming that some demixing objects are created, the scattering profiles at $q_x > q_{mx}$, as already discussed in our previous works,[12,13] should be represented by a linear combination of a squared Lorentzian function (SQL),

$$I_{SQL}(q) = \frac{I_{SQL}(q=0)}{(1 + q^2\Xi^2)^2} \tag{5}$$

which expresses the scattering of the random two-phase structures with a sharp interface and an OZ function (eq 2), which reflects the scattering from the concentration fluctuations inside the respective polymer-rich as well as polymer-poor domains. As is well-known, the SQL function shows on a double-logarithmic scale a plateau region at $q\Xi < 1$, where Ξ is the correlation length of the demixed domains, and a power law (in practice, a straight line corresponding to $I_{SQL} \sim q^{-\alpha}$) with an exponent α of 4 at $q\Xi > 1$. However, the apparent exponents α in $I(q_x)$ and $I(q_z)$ at $\dot{\gamma} > \dot{\gamma}_{c,demix}$ in Figures 5, 6, 8, and 9 display values between 2.4 and 3. This apparent slope can thus be a combination of −4 attributed to SQL at $q\Xi > 1$ and of the plateau or the −2 exponent of the OZ function.

If we only consider the SANS data, the fits with the linear combination of an OZ and a SQL are very satisfactory, although the SQL function gives an exponent $\alpha = 4$ (Figure 11). Nevertheless, since no plateau is visible in a low-q side of the SANS, our data could be fitted with another function, having $\alpha = 3$, for example. It is also intuitively clear that the value of Ξ obtained by the fit with a function having $\alpha = 3$ is larger than the one obtained with a SQL ($\alpha = 4$) because the function will be more spread out. Let us see this in detail below.

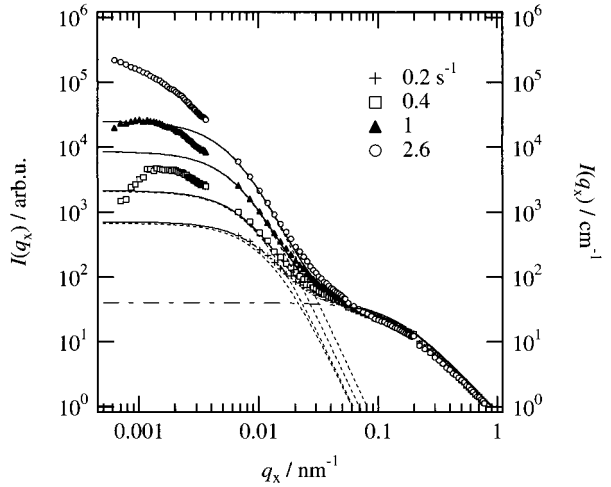

Figure 11. Reproduction of the scattering profiles at 22 °C (shown by solid lines and symbols) by linear combination of a SQL (dashed lines) and an OZ function (dash and dot lines). The values of ξ are the same for all the shear rates (6.86 nm), and the values of Ξ are 82.3 nm (0.2 s^{-1}), 109 nm (0.4 s^{-1}), 137 nm (1 s^{-1}), and 155 nm (2.6 s^{-1}).

Table 2. Parameters Used for the Fitting with Eq 7[a]

T/C°	n_x	n_z	Ξ_x/nm	Ξ_z/nm	ξ_x/nm	ξ_z/nm
12.2	0.16	0.22	316	237	10.2	11.0
15.5	0.16	0.20	339	342	9.34	9.52
17.5	0.22	0.35	313	429	8.64	8.62
22.0	0.32		327		7.48	8.16

[a] n, Ξ, and ξ are respectively the exponent, the correlation length of domains, and the correlation length of the thermal concentration fluctuations inside domains as discussed in the text in conjunction of eq 7.

4.3.2. OZ with a Modified SQL Function. If we now consider the whole q range (SANS and SALS data), a fit with a SQL is not possible, because it would give Ξ too small. To fit over the wide window of q vector covered by combining SALS and SANS, we therefore clearly need an additional function or another function (having $\alpha < 4$) replacing the SQL function.

We modify the correlation function for the SQL function, $g(r) = r^0 \exp(-r/\Xi)$, into $g(r) = r^{-n} \exp(-r/\Xi)$, where n is an exponent between 0 and 1. Fourier transform of this $g(r)$ leads to the following modified SQL function, $I_{\mathrm{mSQL}}(q)$ (see calculation in Appendix 2):

$$I_{\mathrm{mSQL}}(q) \sim \frac{\sin[(2-n)\arctan(q\Xi)]}{q\Xi^{n-2}(1+q^2\Xi^2)^{(1-n/2)}} \qquad (6)$$

This function results in the SQL function for $n = 0$ and the OZ function for $n = 1$, therefore providing an interpolation between the SQL and the OZ function. As n approaches from 0 to 1, the exponent α at $q\Xi > 1$ changes from 4 to 2. From eqs 2 and 6, we finally have the following scattering function:

$$I(q) = K\frac{\sin[(2-n)\arctan(q\Xi)]}{q\Xi^{n-2}(1+q^2\Xi^2)^{(1-n/2)}} + \frac{I_{\mathrm{OZ}}(q=0)}{1+q^2\xi^2} \qquad (7)$$

where K is a numerical factor.

The results of the data fitting by eq 7 are presented in Figure 12, and the fitting parameters obtained are given in Table 2. (The fitted curves are given only for the profiles at $\dot\gamma > \dot\gamma_{\mathrm{c,demix}}$ to which the fitting is properly applicable.) In the whole SANS q region and the high-q region of SALS, the fits are better than the ones obtained with a linear combination of a SQL and an OZ functions. Including the SALS data makes the fit more exact for the determination of n. However, we must remember that an intensity prefactor common to all SALS data has been set arbitrarily and remark that the fit is not perfect at low q. In this q region, we obviously expect a deviation when data are displaying a peak, and an appropriate modification should be done in this very low-q range (we return to that in sec 4.3.3).

In summary, the misfit of a SQL function is clear here, and the relative success of the mSQL suggests that the shear-induced structures responsible for this q region are only quasi-two-phase structures. However, this quasi-two-phase structure is still a demixed object in a sense which will be discussed immediately below.

4.3.3. The Exponent α at Intermediate Q Values. At this stage we would like to compare the data from the steady shear with the one from oscillatory shear.[13] In this latter case, an exponent $\alpha = 4$ is observed, indicating that oscillatory shear flow can drive the system toward the completely phase-separated state characterized by well-defined interfacial boundaries, while steady shear flow does not. This may be associated with the fact that an oscillatory shear flow of fixed frequency selects more precisely one mode in q, i.e., leads to more precise size distribution, whereas continuous shear selects all modes with q smaller than a given value of q, satisfying $\Gamma(q) \le \dot\gamma$[22] where $\Gamma(q)$ is relaxation rate of the Fourier modes with wavenumber q.

More precisely, the fact that α deviates here from 4 (which reflects the sharp interface) might result from the following three possibilities. First, the interfaces of the demixed objects might be fractallike. The interfaces having the surface fractal dimension D_s give the power law region in its scattering function with an exponent of $\alpha = 6 - D_s$. The observed power law exponents, especially in Figures 8 and 9 (temperature dependence at 2.6 s^{-1}), are nearly 3, indicating D_s are also nearly 3. This fractal dimension is somewhat large, which may reflect the extremely rough interface. Second, we should take into account a possibility of the polydispersity effect of the shear-induced structures. For example, physicists of the field of porous media have built various size distribution functions which produce apparent exponents between 2.5 and 4. A serious analysis along those lines would necessitate cross-checks (using other techniques) which are not available at present. Finally, we cannot discard the possibility that the shear-induced demixed structures have internal structures other than thermal concentration fluctuations, without knowing which one. In other words, the internal heterogeneity in the demixed structures would give an excess scattered intensity at the q region where the demixed structures without the internal heterogeneity give the Porod law of q^{-4}, yielding the net scattering from the demixed structures with the internal heterogeneity to have an apparent power law exponent α smaller than 4.

4.3.4. Low-Q Behaviors and Fitting. Returning to the low-q region of SALS, we recall that the curves fitted with a mSQL function as well as the curves fitted with a SQL function show a downward deviation from the observed intensity. This can be related to the existence of a maximum, as seen for the lower shear effect. Crudely speaking, the modified SQL may be suitable at $q > q_{mx}$, where it describes the form factor of the

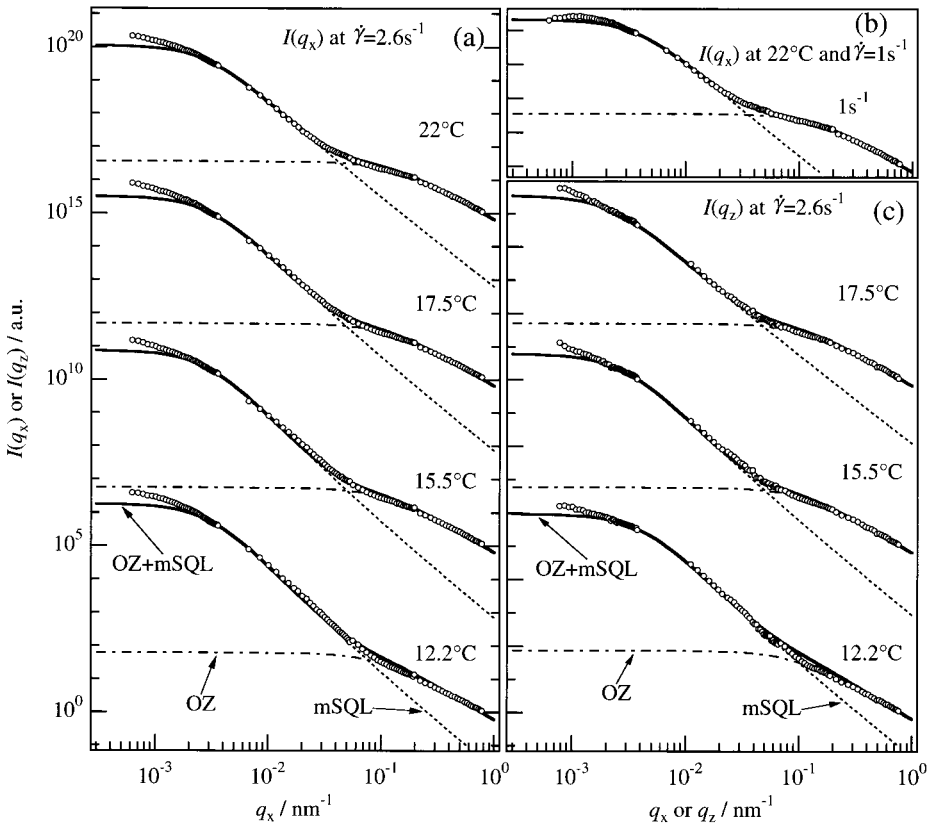

Figure 12. Reproduction of the scattering profiles (shown by solid lines) by a linear combination of a modified SQL (dotted lines) and an OZ function (dash and dot lines): (a) temperature dependence of $I(q_x)$ at 2.6 s^{-1} (appeared in Figures 9 and 10), (b) $I(q_x)$ at 22 °C and 1 s^{-1} (appeared in Figures 6 and 7), and (c) temperature dependence of $I(q_z)$ at 2.6 s^{-1}(appeared in Figures 9 and 10).

demixed objects, while the structure factor at $q \lesssim q_{mx}$ is influenced by interference of scattered light from the demixed objects.

Since this low-q deviation does not allow us to obtain really accurate values of Ξ, we can only look qualitatively at the variation of Ξ as the shear effect is increased. Ξ_x (Ξ parallel to flow) evaluated from the analysis of Figure 5 (a) ($\dot{\gamma}$ dependence at 22 °C) with eq 7 is 248 nm for 1 s^{-1} and 327 nm for 2.6 s^{-1}, indicating that the size of the shear-induced structures increases with $\dot{\gamma}$. This tendency agrees with the results obtained with the SQL + OZ fits and with the shift of the SALS maximum observed at lower shear rates. Note that the exponent n_x (n parallel to flow) in eq 7 is 0.41 for 1 s^{-1} and 0.32 for 2.6 s^{-1}, which would indicate better defined demixed objects at larger $\dot{\gamma}$.

For larger shear effects, (T dependence at $\dot{\gamma} = 2.6$ s^{-1}) the values of Ξ_x and Ξ_z (Ξ perpendicular to flow) estimated from Figure 12 are summarized in Table 2 and Figure 13. Ξ_x takes almost a constant value, and Ξ_z decreases with decreasing temperature, although the scattering intensity at low q increases in both directions with decreasing temperature. At 12.2 °C, Ξ_z becomes even lower than Ξ_x, consistent with and explaining the elliptical SANS pattern with its major axis oriented along z direction (Figure 7). As T decreases, n_x as well as n_z decrease or α increases. These results may reflect an enhancement of the phase separation, with better-defined interfaces between (quasi) two phases.

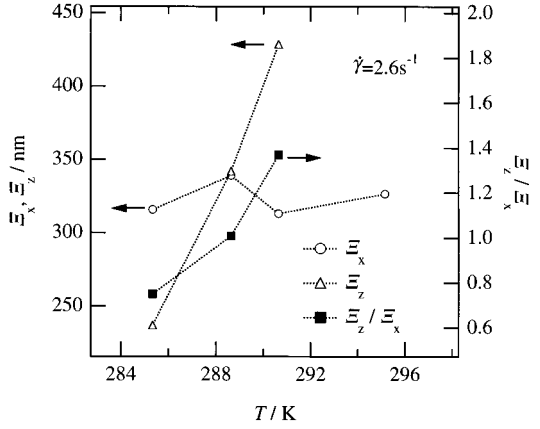

Figure 13. Ξ_x, Ξ_z (left axis) and Ξ_z/Ξ_x(right axis) as a function of temperature T.

5. Discussion

In this section, we finally want to discuss some available theoretical models and compare their predictions with our experimental results. We first describe pioneer models, which predict directly the scattering, though they do not describe our data features. Then we try to discuss the physics of these features, while introducing more recent models, which do not explicitly calculate the scattering but agree much better with our results.

5.1. Helfand−Fredrickson and Milner Models. The theoretical models for solutions under shear have been initiated by Helfand and Fredrickson[1] (HF), who proposed, via a Navier−Stokes equation, to account for coupling between concentration fluctuations and local flow via the concentration dependence of viscosity (see eq A1 in Appendix 1). The increase in intensity by shear stress is predicted only in the q_x-q_y plane, but that in the q_x-q_z plane was not calculated. This can be considered as a perturbation calculation, which could be

suitable to a first stage, i.e., for a moderate $\dot{\gamma}$ ($W_i \leq 1$); at large $\dot{\gamma}$ the theoretical result of I_{mx} diverges, and we are not in the validity range of the theory anymore. Our data showing the modified SQL at low q and increase of the scattering along q_z at large W_i ($\gtrsim$30) demonstrate that the linearized HF model does not apply to the strong shear regimes observed here.

A first attempt at accounting for specific polymer behavior is due to Milner,[2] which considers the rheological plateau behavior and predicts a peak in $I(q)$, at a value q_{mx} such that $Dq_{mx}^2\tau_m = 1$. Such a maximum is observed in some of our data: however, the observed $\dot{\gamma}$ dependence of q_{mx}, i.e., the decrease of q_{mx} with $\dot{\gamma}$, cannot be predicted by Milner. Thus, this second model still corresponds in our opinion to moderate effects, close to the linear regime, at variance with our observations.

5.2. Scenario for Higher Deformation and Comparisons with Recent Models. Therefore, we must consider that if $\dot{\gamma}$ is increased further above, stronger effects must occur and also that, eventually, shear-induced phase separation would be brought about. This is very close to purely elastic effects which have also been observed, and then predicted, a few years ago, following the same reasoning in gels under elongation.[23] In the scheme of solvent squeeze as detailed elsewhere,[13,21] solvent escapes from regions already rich in polymer toward regions poor in polymer. The larger the shear rate, the greater the buildup of the elastic free energy and hence the more the solvent is squeezed from the more entangled regions for relaxation of the elastic free energy buildup. The result is not far from the shear-induced phase separation prediction of Onuki[3] and Doi-Onuki.[29] Finally, computer simulations illustrating the sensitivity of the shear effect to a temperature close to spinodal line showed clear-cut regions of low and high polymer concentration.[3,4] Nevertheless, none of these works predict the scattering of such structure. We therefore only take advantages of them to discuss some of the scattering features observed in this work.

5.3. Scattering Maximum. As remarked earlier, the observed scattering maximum does not display the features predicted by the Milner model: q_{mx} decreases with $\dot{\gamma}$. This confirms that the Milner model is not suitable to our situation, probably because we are in a biphasic advanced state of separation.

The variation with $\dot{\gamma}$ of scattering maximum can be explained via a simple picture: the shear flow has two opposite, competing effects. One is the effect that grows the shear-induced structures (solvent-squeezing mechanism[13,21] as incorporated in Doi−Onuki theory[29] as a driving force for phase separation), and another is the effect that breaks up the overgrown structures. In the q region less than q_{mx}, it is the breakup effect that dominates the structure-formation effect. In the q region between q_{mx} and q_{cx}, where the scattering intensity increases with decreasing q, the driving force for the structure formation is stronger than the breakup effect. As $\dot{\gamma}$ increases, this region is extended to lower q. Such shift of q_{mx} toward smaller q_x might mean that the increment of the driving force with $\dot{\gamma}$ is larger than that of the breaking-up effect.

This observed steady-state scattering function contrasts with a polymer solution or a polymer blend undergoing spinodal decomposition without shear: in this case, as time elapses, q_{mx} approaches 0 and I_{mx} increases, indicating that the system finally achieves macroscopic phase separation. Conversely, we might regard the creation of steady-state structures under shear as an "incomplete phase separation", as pointed out by Onuki et al.[4]

5.4. Comments on Q_{cx}. The kind of crossover, as seen in $I(q)$ with decreasing q, from the high-q OZ behavior of thermal concentration fluctuations into the low-q steep increase due to the biphasic structure is signaled by a change in q dependence of $I(q)$ at a value q_{cx} in Figures 5 and 9. This value seems to weakly depend on $\dot{\gamma}$ and temperature. Let us discuss this from two point of views.

The first point of view is model-dependent, sticking to our modeling of the net scattering given by a weighted sum of SQL + OZ, or mSQL (here let us assume SQL for simplicity), and can be summarized as follows:

(1) The OZ part is shear rate independent: the fact that q_{cx} is of the order of $1/\xi$, or slightly smaller than $1/\xi$ allows us to observe any possible variation of the OZ part with $\dot{\gamma}$, if it existed, not only at high $q > 1/\xi$ but also around $1/\xi$ at the scale which characterizes this contribution.

(2) The SQL part is shear rate dependent. We know that its corresponding correlation length Ξ (therefore its front factor by $\{\Xi(\dot{\gamma})\}^3$) and $\langle\eta^2\rangle$ (representing the mean-squared scattering length fluctuations between the two phases) should vary with $\dot{\gamma}$.

(3) The variation of q_{cx} with shear rate should be a simple consequence of a certain combination of the two contributions SQL and OZ. We first can remark that the effect of Ξ on $I(q)$ at $q > 0.05$ nm^{-1} is extremely small (Figure 5a). Actually, the intensity level in the Porod regime in our data increases with increasing $\dot{\gamma}$, which must mean that $\langle\eta^2\rangle$ increases with $\dot{\gamma}$. We may have the following counter-balancing effects. Upon increasing $\dot{\gamma}$, Ξ increases, which may shift q_{cx} toward smaller values but $\langle\eta^2\rangle$ also increases, which may shift q_{cx} toward larger values. These two effects may keep q_{cx} nearly constant with $\dot{\gamma}$. Note that all this is possible because the OZ contribution is not affected by $\dot{\gamma}$.

The second point of view is independent of model and based on the Rayleigh−Gans[24] scattering theory in the context of Born approximation:[25] The scattering intensity $I(q)$ depends on the intensity of q Fourier modes. However, from a second more general point of view, our observation of nearly constant q_{cx} with $\dot{\gamma}$ may be surprising at a first glance: as $\dot{\gamma}$ increases, q_{cx} should be expected to increase. This is because a shear flow of given $\dot{\gamma}$ affects only Fourier modes of concentration fluctuations with their relaxation rates $\Gamma(q) < \dot{\gamma}$. Since $\Gamma(q)$ increases with q, the modes affected by shear will be the low-q modes satisfying $q < q_{cx}$ where q_{cx} satisfies $\Gamma(q=q_{cx}) \simeq \dot{\gamma}$. They will build up local variations of shear stress and normal stress difference in our solution through the coupling between concentration fluctuations and stress. This coupling involves the solvent-squeeze mechanism, giving rise to the shear-induced enhancement of the concentration fluctuations. At the same time, Fourier modes of $q > q_{cx}$ ($\Gamma(q) > \dot{\gamma}$) relax before they are affected by shear. Therefore, the high-q modes with $q > q_{cx}$, and hence $I(q)$ at $q > q_{cx}$ will not be affected by shear. From a general point of view, when $\dot{\gamma}$ increases, q_{cx} should tend to increase. However, the increase of q_{cx} with $\dot{\gamma}$ may be very small if $\Gamma(q)$ increases very rapidly with q around or above q_{cx}. A good reason for such a fast crossover in $\Gamma(q)$ at $q \simeq q_{cx}$ could be that entanglements slow the relaxation above a certain size ξ_e and hence below a certain $q_e \simeq 1/\xi_e$, where ξ_e is the

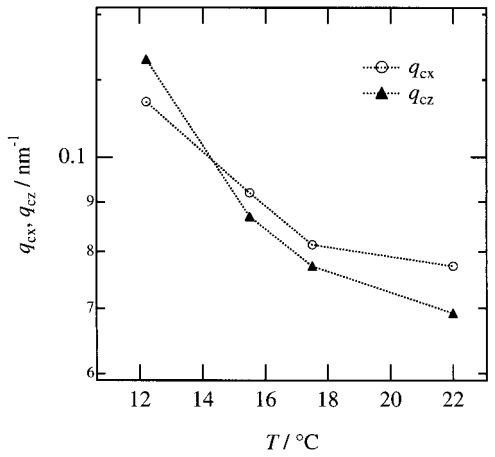

Figure 14. q_{cx} and q_{cz} as functions of T.

average spacing between entanglement points in the semidilute solution. We have then to compare q_{cx} and $1/\xi_e$.

To determine ξ_e, let us introduce the equation proposed by Nemoto et al.,[26] in which the relation between the concentration (c) (g/mL) and the molecular weight between entanglement points (M_e) in a semidilute solution is specified:

$$cM_e = 1.8 \times 10^4 \tag{8}$$

From this equation, M_e in the solution is found to be 2.28×10^5. ξ_e can be determined by the following equation:

$$\xi_e = \sqrt{\frac{M_e}{M_w}\langle R^2\rangle} \tag{9}$$

where $\langle R^2\rangle$ is the mean-squared end-to-end distance of the polymer chain. In this calculation, we postulate that $\langle R^2\rangle$ hardly depends on temperature in the range covered in this experiment, and then the value estimated by $\langle R^2\rangle = N_w b^2$ is used, where b is the statistical segmental length and N_w is the weight-average degree of polymerization. The value ξ_e in this solution with 8.0 wt % polymer concentration is estimated to be ca. 31.4 nm over the temperature range covered in this experiment. Similar values of M_e can be found in papers of Graessley et al.[27] and Adam et al.[28] In summary, from these estimates, we observe that $1/\xi_e$ might be substantially smaller than q_{cx}, giving rise to $1/\xi_e < q_{cx} < 1/\xi$. (The corresponding $1/\xi_e$ values are indicated by the arrows in Figure 5.) This well explains why the OZ contribution remains constant with $\dot\gamma$. This can explain also why the values of Ξ are large, since they must be larger than ξ_e. The fact that they have little effect on q_{cx} can be linked to a distribution of sizes comprised between a maximum value Ξ, and a cutoff fixed value, ξ_e, which influences the scattering up to q_{cx}, via a modified SQL accounting for this distribution. This is a starting point for harmonizing the two points of view.

Let us finally look at the case where the temperature is decreased: we can expect that the decrease in T slows down the dynamics of fluctuations $\Gamma(q)$ and therefore is equivalent to an increase of $\dot\gamma$ and thus to an increase of q_{cx}. This is observed experimentally, though the increase is small here again, as shown in Figure 14.

5.5. Influence of Temperature and Molecular Weight. When T is lowered, the system is closer to phase separation at rest. Therefore, it is expectable that it will be more sensitive to demixing. When T is reduced, as remarked already for smaller molecular weight,[12] shear-induced phase separation occurs at lower $\dot\gamma$ but also at lower W_i; this is partly due to change in rheological properties (e.g., an increase in η_0) and partly due to the critical slowing down of concentration fluctuations on approaching the spinodal line.

Such sensitivity to temperature close to spinodal line is illustrated in Onuki's works[3,4] by virtual photos as already mentioned. Such pictures are very close from our description here: they clear-cut regions of low and high polymer concentration obtained have various shapes and a broad distribution of sizes.

The effect of molecular mass as illuminated by comparing the present work with our former work can also be explained in the line of phase separation: sensitivity to phase separation is much larger for large molecular weight. If molecular weight is lower, the chains are still small enough to be insensitive, and the system demixes at higher $\dot\gamma$. Higher W_i are necessary for well-defined effects.

Finally, the fact that larger chains are more entangled, may enhance elastic effects. This could explain also the effect of M_w and would be a support for the explanation involving not only the viscous effect but also the elastic effect.

6. Summary

We have conducted SALS and SANS experiments in order to investigate the structures in a semidilute d-PS/DOP solution developed under steady shear flow. The $\dot\gamma$ dependence of the structures at a given temperature and the temperature dependence of the structures at a given $\dot\gamma$ were investigated over a wide q range in the q_x-q_z plane.

At a given temperature, the dependence of SALS and SANS was found to fall into two regimes: regime I at $\dot\gamma < \dot\gamma_c$, where the scattering in the q_x-q_z plane was that of the quiescent solution, and regime II, where butterfly patterns appeared and were developed with increasing $\dot\gamma$ in both SALS and SANS. At a given $\dot\gamma$, the butterfly evolved further as temperature decreases, resulting in an elliptical scattering pattern with a major axis perpendicular to the flow direction in the low-q region of SANS.

The obtained scattering profiles at $\dot\gamma > \dot\gamma_{c,demix}$ (the critical shear rate for the shear-induced demixing, the signature of which is given by the excess scattering along q_z) and at $q_x > q_{mx}$ could be decomposed into two scattering functions: the modified SQL function, reflecting the quasi-random two-phase structures, and the OZ function, reflecting the concentration fluctuation inside the respective domains. This analysis suggested three possible different shear-induced domain features: surface fractality, polydispersity in size, and internal structures. Since this shear-induced scattering was not predicted by models, only qualitative comparison has been done with theoretical work.

As we already elucidated in many places in this paper, though qualitatively, the observed scattering structure factors in the q_x-q_z plane at $W_i \gtrsim 1$ involve the nonlinear effects in the time evolution behavior of the shear-induced concentration fluctuations or structures. Thus, the observed scattering functions, which were

found to be described phenomenologically by a weighted sum of the modified SQL function and the OZ function, disagree with the first predictions of HF and Milner[1,2] and cannot be predicted by the linearized versions[30,31] of the original nonlinear time evolution equation,[1−3,29] as fully described elsewhere.[32] Our observed scattering functions should be compared with those predicted by computer simulations in three-dimensional space based upon the original nonlinear time evolution equations[1−3,29] with a proper incorporation of space- and time-dependent stress terms, since the nonlinear time evolution equations cannot be solved either analytically or numerically. However, this comparison is beyond scope of the present paper and hence left as future works.

Appendix 1. Remarks on Observation of Scattering in the q_x-q_z Plane and in the q_x-q_y Plane

Up to now basic physics in the systems that have been discussed here are described theoretically in the q_x-q_y plane, i.e., the plane composed of velocity and velocity gradient, since this plane is considered to be the plane where the creation, convection, and death of the fluctuations can be seen most directly in shear flow. However, the scattering in this q_x-q_y plane is experimentally very difficult to be obtained, especially from a viewpoint of obtaining quantitative data with high accuracy. On the other hand, the scattering in the velocity−vorticity plane (q_x-q_z plane) is easier to be accessed than that in the q_x-q_y plane, and quantitative data with high accuracy can be more easily obtained. Below we would like to point out that the scattering in the q_x-q_z plane reflects in principle the same physical factors as the scattering in the q_x-q_y plane, against our intuition, in the context of the linearized dynamical equation.

According to the Helfand-Fredrickson, Milner, and Onuki the dynamical equation of the concentration fluctuations which accounts for the stress-diffusion coupling is given by[1−3,29]

$$\left(\frac{\partial}{\partial t}+\mathbf{v}\cdot\nabla\right)\phi=\nabla\cdot L\left[\nabla\frac{\delta F}{\delta\phi}-\frac{1}{\phi}\nabla\cdot\boldsymbol{\sigma}^{(n)}\right] \tag{A1}$$

where $\mathbf{v}$ is the average velocity of the polymer and the solvent, ϕ the volume fraction of polymer, L the Onsager coefficient, F the free energy functional, and $\boldsymbol{\sigma}^{(n)}$ the network stress tensor. Starting from this general nonlinear time evolution equation and linearizing it in terms of concentration fluctuations, we obtain the following simplified equation for the steady-state scattering function,[33]

$$I(\mathbf{q})=\int_0^\infty \mathrm{d}s\; 2L|\mathbf{k}(s)|^2\exp[-2\int_0^s \mathrm{d}t\;\Gamma(\mathbf{k}(t))] \tag{A2}$$

$$\mathbf{k}(t)=\mathbf{q}+\dot\gamma t q_x\mathbf{e}_y \tag{A3}$$

$$\Gamma(\mathbf{q})=L\left\{q^2(r_0+Cq^2)-\frac{1}{\phi}\left[2q_xq_y\left(\frac{\partial\sigma_{xy}}{\partial\phi}\right)+\frac{1}{3}(2{q_x}^2-{q_y}^2-{q_z}^2)\left(\frac{\partial N_1}{\partial\phi}\right)\right]\right\} \tag{A4}$$

where $\mathbf{e}_y$ is the unit vector along the y axis, r_0 is the second derivative of the Flory−Huggins free energy density for a semidilute solution with respect to ϕ, the coefficient C is related to the gradient free energy, σ_{xy} is the shear stress, and N_1 is the first normal stress difference. The detailed calculations leading to eqs A2 and A3 will be given elsewhere.[32]

On the basis of the simplified eqs A2−A4, we can compare the scattering intensity at a particular point of $q_x=q_y=q$ in the q_x-q_y plane, $I(q,q,0)$, and that at $q_x=q_z=q$ in the q_x-q_z plane, $I(q,0,q)$.

$$I(q,q,0)=\int_0^\infty \mathrm{d}s\; 2L[1+(1+\dot\gamma s)^2]q^2\exp\{-2\int_0^s \mathrm{d}t\;\Gamma[\mathbf{k}(t)]_{\text{at } q_x=q_y=q}\} \tag{A5}$$

$$\Gamma[\mathbf{k}(t)]_{\text{at } q_x=q_y=q}=Lq^2\left\{[1+(1+\dot\gamma t)^2](r_0+C[1+(1+\dot\gamma t)^2]q^2)-\frac{1}{\phi}\left[2(1+\dot\gamma t)\left(\frac{\partial\sigma_{xy}}{\partial\phi}\right)+\frac{1}{3}[2-(1+\dot\gamma t)^2]\left(\frac{\partial N_1}{\partial\phi}\right)\right]\right\} \tag{A6}$$

$$I(q,0,q)=\int_0^\infty \mathrm{d}s\; 2L[2+(\dot\gamma s)^2]q^2\exp\{-2\int_0^s \mathrm{d}t\;\Gamma[\mathbf{k}(t)]_{\text{at } q_x=q_z=q}\} \tag{A7}$$

$$\Gamma[\mathbf{k}(t)]_{\text{at } q_x=q_z=q}=Lq^2\left\{[2+(\dot\gamma t)^2](r_0+C[2+(\dot\gamma t)^2]q^2)-\frac{1}{\phi}\left[2\dot\gamma t\left(\frac{\partial\sigma_{xy}}{\partial\phi}\right)+\frac{1}{3}[1-(\dot\gamma t)^2]\left(\frac{\partial N_1}{\partial\phi}\right)\right]\right\} \tag{A8}$$

Comparison of eqs A5 and A6 with eqs A7 and A8 may clarify that $I(q,q,0)$ and $I(q,0,q)$ reflect essentially identical physical factors, though the thermodynamic terms (the first term of the rhs of eqs A6 and A8) and the stress terms (the second term of rhs of eqs A6 and A8) contribute differently to $I(q,q,0)$ and $I(q,0,q)$.

Appendix 2

We define a correlation function for the modified squared Lorentzian function as

$$g(r)=r^{-n}\exp\left(-\frac{r}{\Xi}\right) \tag{A9}$$

The scattering intensity is given by

$$I(q)=\int_0^\infty 4\pi r^2 g(r)\frac{\sin(qr)}{qr}\,\mathrm{d}r \tag{A10}$$

$$=\frac{4\pi}{q}\int_0^\infty r^{1-n}\exp\left(-\frac{r}{\Xi}\right)\sin(qr)\,\mathrm{d}r \tag{A11}$$

Making use of the trigonometrical function

$$\sin\theta=\frac{\exp(i\theta)-\exp(-i\theta)}{2i} \tag{A12}$$

and the integral formula

$$\int_0^\infty x^{\nu-1}\exp[-(a+ib)x]\,\mathrm{d}x=\Gamma(\nu)(a^2+b^2)^{-\nu/2}\exp\left[-i\nu\arctan\left(\frac{b}{a}\right)\right] \tag{A13}$$

yields the following modified squared Lorentzian function:

$$I(q) = \frac{2\pi}{iq}\int_0^\infty r^{1-n}\left[\exp\left[-\left(\frac{r}{\Xi} - iqr\right)\right] - \exp\left[-\left(\frac{r}{\Xi} + iqr\right)\right]\right] \mathrm{d}r \quad \text{(A14)}$$

$$= \frac{2\pi}{iq}\Gamma(2-n)(\Xi^{-2} + q^2)^{-1+n/2}[\exp[-i(2-n) \arctan(-q\Xi)] - \exp[-i(2-n)\arctan(q\Xi)]] \quad \text{(A15)}$$

$$= K\frac{\sin[(2-n)\arctan(q\Xi)]}{q\Xi^{n-2}(1+q^2\Xi^2)^{(1-n/2)}} \quad \text{(A16)}$$

where K is a constant for a given n.

References and Notes

(1) Helfand, E.; Fredrickson, G. H. *Phys. Rev. Lett.* **1989**, *62*, 2468.
(2) Milner, S. T. *Phys. Rev. E* **1993**, *48*, 3674.
(3) Onuki, A. *J. Phys.: Condens. Matter.* **1997**, *9*, 6119.
(4) Onuki, A.; Yamamoto, R.; Taniguchi, T. *J. Phys. II* **1997**, *7*, 295.
(5) Hashimoto, T.; Fujioka, K. *J. Phys. Soc. Jpn.* **1991**, *60*, 356.
(6) Wu, X.-L.; Pine, D. J.; Dixon, P. K. *Phys. Rev. Lett.* **1991**, *66*, 2408.
(7) Hashimoto, T.; Kume, T. *J. Phys. Soc. Jpn.* **1992**, *61*, 1839.
(8) Kume, T.; Hattori, T.; Hashimoto, T. *Macromolecules* **1997**, *30*, 427.
(9) van Egmond, J. W.; Werner, D.; Fuller, G. G. *J. Chem. Phys.* **1992**, *96*, 7742.
(10) Dixon, P. K.; Pine, D. J.; Wu, X.-L. *Phys. Rev. Lett.* **1992**, *68*, 2239.
(11) Boué, F.; Lindner, P. *Europhys. Lett.* **1994**, *25*, 421.
(12) Morfin, I.; Lindner, P.; Boué, F. *Macromolecules* **1999**, *32*, 7208.
(13) Saito, S.; Koizumi, S.; Matsuzaka, K.; Suehiro, S.; Hashimoto, T. *Macromolecules* **2000**, *33*, 2153.
(14) Kume, T.; Hashimoto, T.; Takahashi, T.; Fuller, G. G. *Macromolecules* **1997**, *30*, 7232.
(15) The polymerization proceeded under a normal condition, and hence we expect heterogeneity index of d-PS satisfies $M_w/M_n \lesssim 1.1$.
(16) c^* was calculated using $c^* = 3M_w/(4\pi R_g^3 N_A)$ with $R_g = b(N_w/6)^{0.5}$, where R_g, N_A, b, and N_w are respectively the radius of gyration of a single polymer molecule, Avogadro's number, the statistical segmental length, and the weight-average degree of polymerization.
(17) Matsuzaka, K.; Hashimoto, T. *Rev. Sci. Instrum.* **1999**, *70*, 2387.
(18) Lindner, P.; Oberthür, R. *Colloid Polym. Sci.* **1985**, *263*, 443.
(19) Bird, R. B.; Armstrong, R. C.; Hassager, O. *Dynamics of Polymeric Liquids*; Wiley: New York, 1977.
(20) Saito, S.; Hattori, T.; Hashimoto, T., manuscript in preparation.
(21) Saito, S.; Hashimoto, T. *J. Chem. Phys.* **2001**, *114*, 10531.
(22) Saito, S.; Hashimoto, T.; Pine, D., manuscript in preparation.
(23) Mendes, E.; Lindner, P.; Buzier, M.; Boué, F.; Bastide, J. *Phys. Rev. Lett.* **1991**, *12*, 1595.
(24) Van de Hulst, H. C. *Light Scattering by Small Particles*; J. Wiley & Sons: New York, 1957.
(25) Born, M. *Z. Phys.* **1926**, *37*, 863; **1926**, *38*, 803.
(26) Nemoto, N.; Kishine, M.; Inoue, T.; Osaki, K. *Macromolecules* **1991**, *24*, 1648.
(27) Graessley, W. W. *Advances in Polymer Science*; Springer-Verlag: Berlin, 1974; Vol. 16.
(28) Adam, M.; Farago, B.; Schleger, P.; Raspaud, E.; Lairez, D. *Macromolecules* **1998**, *31*, 9213.
(29) Doi, M.; Onuki, A. *J. Phys. II* **1992**, *2*, 1631.
(30) Ji, H.; Helfand, E. *Macromolecules* **1995**, *28*, 3869.
(31) van Egmond, J. W. *Macromolecules* **1997**, *30*, 8045.
(32) Saito, S.; Takenaka, M.; Toyoda, N.; Hashimoto, T. *Macromolecules* **2001**, *34*, 6461.
(33) Onuki, A.; Kawasaki, K. *Ann. Phys. (N.Y.)* **1979**, *121*, 456; **1981**, *131*, 217.

MA002051M